Granular labyrinth structures in confined geometries

Henning Arendt Knudsen,* Bjørnar Sandnes, Eirik Grude Flekkøy, and Knut Jørgen Måløy
Department of Physics, University of Oslo, P.O. Box 1048 Blindern, NO-0316 Oslo, Norway
(Received 9 October 2007; published 5 February 2008)

Pattern forming processes are abundant in nature. Here, we report on a particular pattern forming process. Upon withdrawal of fluid from a particle-fluid dispersion in a Hele-Shaw cell, the particles are shown to be left behind in intriguing mazelike patterns. The particles, initially being uniformly spread out in a disc, are slowly pulled inwards and together by capillary and pressure forces. Invading air forms branching fingers, whereas the particles are compiled into comparably narrow branches. These branches are connected in a treelike structure, taking the form of a maze. The characteristic length scale within the structure is found to decrease with the volume fraction of the particles and increase with the plate separation in the Hele-Shaw cell. We present a simulator designed to simulate this phenomenon, which reproduces qualitatively and quantitatively the experiments, as well as a theory that can predict the observed wavelengths.

DOI: 10.1103/PhysRevE.77.021301 PACS number(s): 45.70.Qj, 47.20.Ma, 47.54.−r, 89.75.−k

I. INTRODUCTION

Systems driven out of equilibrium tend to spontaneously form patterns on length scales much larger than their individual constituents. Complex shapes and structures emerge in self-organized processes governed by simple rules executed repeatedly and in parallel across space [1]. Examples of pattern formation in nature are numerous: dunes and ripples in windblown sand, fracture patterns, dendritic growth of crystals and plants, and the growth of fractal river networks over geological time scales, to mention but a few [2,3].

A large variety of patterns exists, yet one also finds that seemingly unrelated processes may produce patterns with similar characteristics [4]. The formation of diffusion limited aggregation (DLA) clusters, for instance, is fundamentally related to viscous fingering in consolidated porous media [5]. In order to characterize the pattern formation process, one needs to identify the different mechanisms that govern its behavior, and reveal the often subtle interplay between the competing forces in the system.

In this paper we demonstrate and characterize a pattern forming process where random, labyrinthine structures emerge from the slow drying of fluid-grain mixtures in confined geometries [6]. Experiments and simulations reveal that the interface instability develops as a compromise between capillary forces and friction, and we present an analytic prediction of the observed characteristic length scales in the patterns. The grain labyrinth bears visual resemblance to patterns formed in other systems such as chemical reaction-diffusion processes [7,8] and magnetic and dielectric fluids under external fields [9]. Labyrinthine patterns have also been observed in other drying processes which have been studied experimentally [10] and using lattice models [11].

As the fluid is gradually drained from the cell, the fluid-air interface at the perimeter of the circular disc starts to recede. The capillary forces between the wetting fluid and the grains gradually compile a growing layer of close-packed grains ahead of the interface as it moves. After an initial transient period where a compact layer of grains is formed all along the circular perimeter, an instability develops whereby the fluid-grain disc is slowly invaded by fingers of air. Figure 1 shows consecutive images of this process, where one can observe the gradual advance and splitting of fingers, resulting in the complex, labyrinthine pattern seen in the fully drained cell. Unlike drying processes where individual pinning plays a role [10,12,13], the finger splitting is due to a collective jamming of the interface on a length scale larger than the individual grains. The time sequence by which the pattern is formed is not discernible in the final pattern. The grains, originally uniformly distributed, have been reorganized by the stretching interface into a long, thin, branching structure of close-packed particles separated by wider paths. Each branch is assembled from the compact layer of grains pushed ahead by two adjoining fingers of air. For example, in the experiment shown in Fig. 1, the initial circular perimeter is approximately 1 m long, and the circumference of the final cluster measures 13.3 m.

II. EXPERIMENTAL SETUP AND PROCESS

The confined geometry studied is a Hele-Shaw cell [14], which extends 50 cm×50 cm (see Fig. 2). The upper and lower glass plates are 10 mm thick, which assures that they bend very little under their own weight. By means of eight spacers, the gap between the plates is well defined and can be freely chosen. The cell is mounted in a frame with three

FIG. 1. (Color online) The figure shows five consecutive photos of the experiment: four during the process (after 3, 11, 28, and 42 h) and one after completion. Black areas are air filled, the bright areas are either branches of compacted grains or areas with fluid above a layer of grains, which are not yet drained. Each picture frame is 40×40 cm.

*hak@fys.uio.no

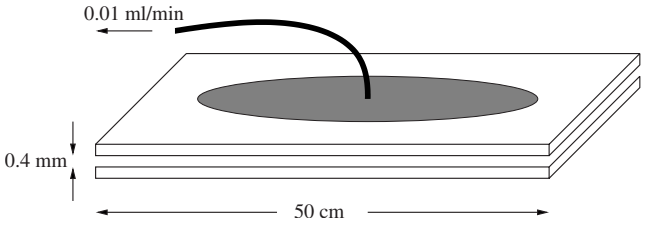

FIG. 2. Sketch of the experimental setup: Two 50 cm $\times$ 50 cm $\times$ 10 mm glass plates are placed horizontally above each other with an adjustable but well defined spacing between them. A hole drilled through the central point of the top plate serves as the injection point and the extraction point for fluid-particle mixture and fluid, respectively.

adjustment screws resting on a table such that the cell can be leveled accurately. A square "window" is cut in the table allowing imaging from underneath where no tubes or other equipment block the view. The upper glass plate is pressed downwards by its own weight and by eight additional weights that are placed directly above each of the spacers. This is preferred to clamping the plates together because the latter method can cause the plates to bend.

The drying or draining process that we have studied starts from a circular disk of particle-fluid mixture between the glass plates. The particles are heavier than the fluid and therefore initially rest on the lower glass plate. Here we have studied glass beads with diameter 50–100 μm, but other particles may be used as long as they sediment out and are wet by the fluid. We have chosen to use a 50/50% glycerol and water mixture as fluid. The reason is that the filling of the cell is done by injecting the fluid quickly through a central hole in the top plate. The fluid must be viscous enough that the particles stay in suspension until the desired size of the disc is reached. Only then the particles should sediment out, and in this way a uniform particle distribution is obtained. Finally, a small portion of extra glass beads is added through the tubing in order to create a small disc of diameter 2 cm below the inlet and outlet point. This prevents the air front to sweep by the outlet prematurely during the experiment.

In order to make the experiment resemble a drying process, the system is drained through the central point at a very low rate. The experiment typically takes two to three days to complete. The fluid is withdrawn into a syringe which is attached to a step motor that is set at constant speed. As the fluid is withdrawn pressure is reduced in the fluid causing the air-fluid interface to recede. As the process is very slow, the motion of the interface is likely to be where it is less hindered. The fluid wets the glass beads, thus the beads are dragged along with the interface. This leads to a compaction of grains inside of the interface and eventually the beads start to pile on top of each other. The increased mass of the pile of beads causes the friction to increase locally. After a short transient we observe a compacted layer of grains along the entire air-fluid interface. The particles are no longer just piling on top of each other but they span the entire gap between the plates. They constitute more or less a block that has to be moved as a whole, and friction is active against both the bottom plate and the top plate.

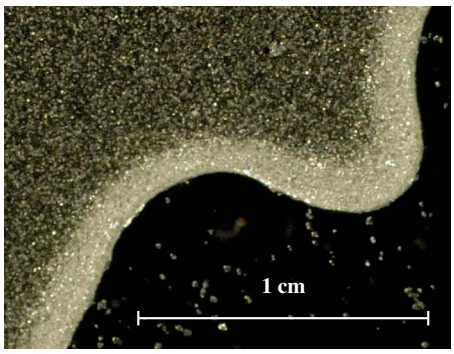

FIG. 3. (Color online) Detailed photo of a segment of the front. The dense region of particles (bright stripe) makes up the front, and the upper left part consists of fluid and particles spread out. Air is outside the front on the lower right side (dark region).

At this stage the pattern formation starts. Capillary forces pull the particles inwards and the friction holds them back. Details follow in Sec. III, but for now observe how the pattern evolves in Fig. 1. Fingers of air invade from the sides into the disc. They roughly have the same width independent of position within the disc and time elapsed. There is no obvious direction of the finger growth. Upon growing, the air fingers push beads in front of themselves and to the side. In this way, the fluid is drained, whereas a residue of particles is left behind. The final grain structure is simply connected in a treelike shape. If one wishes, the grains correspond to the hedges of a garden labyrinth and the air is the footpaths in between.

The rightmost labyrinth structure in Fig. 1 is fully developed, which allows some immediate observations to be made. First, remote areas of fluid like the lower segment in the fourth panel in Fig. 1 have been drained through a long and narrow branch of grains. It is indispensable that the process is slow since in this case D'arcy's law predicts an otherwise large pressure drop over this long and narrow branch. Pinch-offs or air breakthrough into the outlet tube in the middle could otherwise occur and end the experiment prematurely. Second, the mass transport during the process is local. The branches have roughly the same width over the disc, as do the air branches. This reflects the initial state of evenly distributed grains.

III. MODEL DESCRIPTION OF THE RELEVANT FORCES

In order to model the system through simulations, it is necessary to start with a model of the forces involved. The algorithm for the simulations will be based on a statement of balance between these forces.

Seeking a better understanding of the experimental process described in Sec. II, it is useful to look at a closeup photo of an air finger during displacement, see Fig. 3. In this particular case the width of the front is roughly 20 particles. Its motion is from the lower right to the upper left, meaning that the front gathers mass on the upper left hand side as new area is swept over. We observe that on this side there is some fluctuation in the front boundary. This is not the case on the lower right side, the surface towards air. The capillary ten-

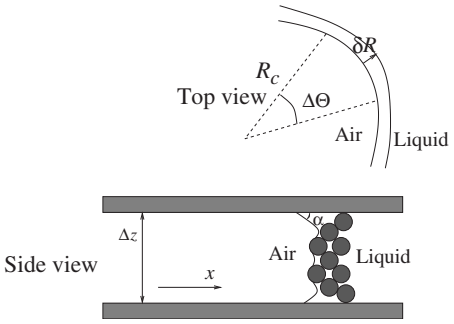

FIG. 4. Part of an air-suspension interface. The particles at the interface are partially exposed to the air, and between them there is a complex surface of constant mean curvature corresponding to the pressure drop ΔP.

sion acts not only as the driving force moving the front, but also to smooth the front. Even though the particles protrude the meniscus a little bit locally (which they must, otherwise no force could act on them), the meniscus is a smooth curve on the scale of many particles.

There are some possible candidates for dominating forces or effects in the problem: surface tension, viscous forces, inertia effects, shear forces in the packing, individual pinning of grains, and friction against the glass plates. Due to the low flow rate, the viscous forces that govern viscous fingering processes are negligible in this case. The same goes for inertia effects. Further, most of the time, the motion of the front implies elongating the front. If shearing were to contribute significantly to resistance against motion it would be expected to be due to dilatancy, but the elongation counteracts this effect. Individual pinning of particles will occur when the plate spacing is close to the size of the largest grains. We have chosen to keep the spacing large enough that this does not happen in this study. This leaves us with two prominent candidates in addition to the pressure forces: friction and surface tension. The correctness of these estimates has *a posteriori* been confirmed by implementing them into a simulator.

A. Capillary forces

We consider a front segment that is short enough to have a well defined curvature R_c in the in-plane direction, as shown in Fig. 4. This segment corresponds to part of the front shown in Fig. 3. It consists of both fluid and particles, some of which reside on the fluid-air interface. We imagine that the pressure is increased so as to create a displacement as illustrated in Fig. 4. In order to identify the forces acting across this interface we consider the work done by the pressure difference ΔP across it, or, more precisely, the work done by the air on the rest of the system. In the quasistatic limit, where we can neglect viscous forces, this work will go into increasing the surface energies and displacing the particle packing. It may be written

$$\Delta P \delta V = \gamma \delta A_f + \Delta\gamma_p \delta A_p + \Delta\gamma_w \delta A_w + \sigma \delta V, \tag{1}$$

where σ is the average stress acting through the particle packing—or rather the component σ_{xx} of this stress—γ is the air-liquid free energy per area (i.e., the surface tension), $\Delta\gamma_w$ is the difference between the air-solid and liquid-solid free energy per area at the wall, $\Delta\gamma_p$ is the corresponding quantity for the particle material, A_w and A_p are the wall and particle surfaces exposed to the air.

In order to interpret the first two right hand side terms of Eq. (1) we now introduce the specific surface areas $a(\Delta P) = A_f/(\Delta z \Delta\Theta R_c)$ and $a_p(\Delta P) = A_p/(\Delta z \Delta\Theta R_c)$. These quantities depend on ΔP since an increase in the pressure will drive the fluid interface into the pores between the particles and change both A_f and A_p. Writing $A_f = a(\Delta P)\Delta z \Delta\Theta R_c$ we see that the area change

$$\delta A_f = \Delta z \Delta\Theta (a\,\delta R + R_c \delta a) \tag{2}$$

has two terms. The first term corresponds to the displacement of the front as a whole the distance δR, and the second to the displacement of the interface into the pores. In fact, we may imagine that the total displacement process is split into two steps: In the first step $R_c \to R_c + \delta R$ at fixed a and a_p, and the corresponding volume and area changes are

$$\delta\bar{V} = \Delta z \Delta\Theta R_c \delta R,$$

$$\delta\overline{A_f} = a \Delta z \Delta\Theta\, \delta R,$$

$$\delta\overline{A_p} = a_p \Delta z \Delta\Theta\, \delta R. \tag{3}$$

In the second step there is no grain displacement, i.e., R_c is fixed, and the fluid interfaces displace a characteristic distance δx into the pores. Since the pore size is much smaller than R_c we are free to assume that $\delta x \ll \delta R_c$. The corresponding volume and area changes are $\delta V' \propto \delta x$, $\delta A_f' = \delta a \Delta z \Delta\Theta R_c$, and $\delta A_p' = \delta a_p \Delta z \Delta\Theta R_c$. In other words, the first and second steps correspond to the large and small scale displacements, respectively. The work corresponding to the second step is

$$\Delta P \delta V' = \gamma \delta A_f' + \Delta\gamma_p \delta A_p'. \tag{4}$$

Subtracting Eq. (4) from Eq. (1) we get the work done by the first step,

$$\Delta P \delta\bar{V} = \gamma \delta\bar{A}_f + \Delta\gamma_p \delta\bar{A}_p + \Delta\gamma_w \delta A_w + \sigma \delta V, \tag{5}$$

where $\delta A_w = 2\Delta\Theta R_c \delta R$. Since $\delta V'/\delta\bar{V} \sim \delta x/\delta R \ll 1$, we conclude that $\Delta P \delta V' \ll \Delta P \delta\bar{V}$ and that the work of the second step may be ignored altogether. This means that, in this approximation, the entire work is in fact given by Eq. (5).

Dividing Eq. (5) through by $\delta\bar{V}$ and using the fact that $\delta\bar{V} \approx \delta V$ as well as the expressions for $\delta\overline{A_f}$ and $\delta\overline{A_p}$ gives us

$$\Delta P = \frac{(a + a_p \cos\alpha_p)\gamma}{R_c} + \sigma + \frac{2\Delta\gamma_w}{\Delta z}, \tag{6}$$

where we have also used Young's law $\Delta\gamma_p = \gamma \cos\alpha_p$, where α_p is the contact angle on the particle surface, to get rid of $\Delta\gamma_p$. This is the result we require.

The last constant term of Eq. (6) we may absorb in ΔP as it will not affect the dynamics of our system. The $(a + a_p \cos\alpha_p)$ prefactor is of the order 1, and may be absorbed

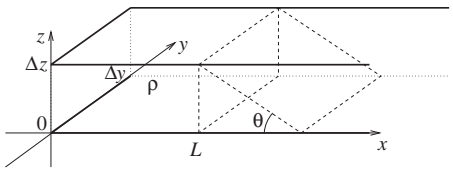

FIG. 5. Sketch of front section of particles between two plates.

in γ to give a new effective surface tension γ'. In the modeling, however, we shall simply make the replacement $(a+a_p\cos\alpha_p)\rightarrow 1$, thus effectively introducing an uncertainty in the surface tension. Note, however, that our approximation will tend to be a good one when particles are barely exposed $(a_p\approx 0)$ and the interface is locally flat $(a\approx 1)$. The photo in Fig. 3 indicates that the particles are not strongly exposed.

B. Friction in the particle front

Having established a capillary force law we now formulate the interface particle stress σ in terms of friction forces. The front, having been compacted to some extent into the shape sketched in Fig. 5, consists of many particles in the two in-plane directions and several particles in the vertical direction. Thus on the mesoscopic scale a Janssen description of the stress in the packing is a good approximation to the actual stress tensor [15].

There, the free surface to the left of the front pushes the front inwards (to the right). The basic idea is that if friction is overcome, motion of the front results.

Taking the principal axes of the stress tensor to lay parallel with the coordinate axes gives

$$\sigma_{zz}=\kappa\sigma_{xx}, \tag{7}$$

where κ is Janssen's proportionality constant. The stress in the y direction is assumed equal to that in the x direction, however, this stress does not enter into the subsequently described equations of motion. We ignore any z dependence of σ and assume translational symmetry in the y direction, from which it follows that $\sigma_{xx}=\sigma_{xx}(x)$, and we make the identification $\sigma_{xx}=\sigma$ with the notation above.

The force balance equation of a vertical differential slice in the x direction is

$$[\sigma(x)-\sigma(x+dx)]\Delta y\Delta z-\mu\sigma_{zz}(x)2\Delta y dx-g\rho\Delta y\Delta z dx\mu=0, \tag{8}$$

when friction is fully mobilized. Here ρ is the mass density of the particle packing. Replacing the σ_{zz} with the help of Eq. (7) and some manipulation gives

$$\frac{d\sigma(x)}{dx}=-\frac{2\mu\kappa\sigma(x)}{\Delta z}-g\rho\mu. \tag{9}$$

This differential equation is valid for the block of particles between the open boundary at $x=0$ and the innermost point, $x=L$, where the packing spans the gap between the planes. At $x=L$ we assume the block to be held back by the excess mass inside, modeled as a triangle,

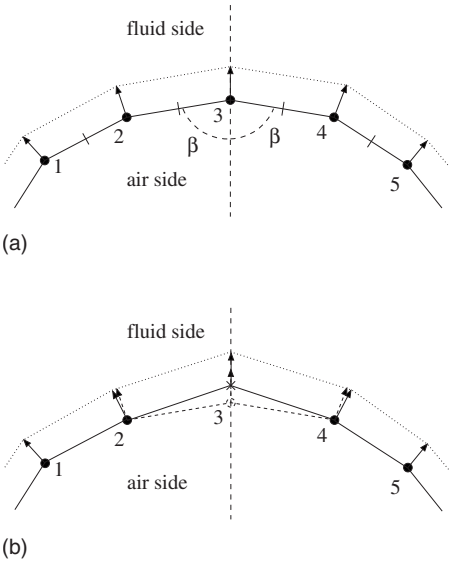

FIG. 6. Five points on the front are shown. For each point the direction normal to the front is drawn as a vector of length corresponding to front thickness L. The orientation, the curvature, and the front thickness change after a move. For clarity in the drawing the displacement in a single move is exaggerated.

$$m_{\rm tr}=\frac{\rho\Delta y(\Delta z)^2}{2\tan\theta}, \tag{10}$$

and the force balance at $x=L$,

$$\sigma(L)\Delta z\Delta y=m_{\rm tr}g\mu. \tag{11}$$

The solution of Eq. (9) becomes

$$\sigma(x)=\frac{g\rho\Delta z}{2\kappa}\left[\left\{\frac{\kappa\mu}{\tan\theta}+1\right\}\exp\left(\frac{2\mu\kappa[L-x]}{\Delta z}\right)-1\right]. \tag{12}$$

We emphasize that this is the limiting case where friction is fully mobilized, which means that the stress $\sigma(x=0)$ is the limiting stress on the open boundary. Higher stress will lead to motion.

C. Simulations

In the simulations the air-liquid pressure force is increased until somewhere along the interface it exceeds the sum of the local capillary and friction forces. The front is then moved a tiny step in the normal direction at that point, and the procedure is repeated. In other words, the point on the interface, which is displaced, minimizes

$$\sigma+\frac{\gamma}{R_c}. \tag{13}$$

The model is based on a one-dimensional representation of the interface, where thousands of consecutive points discretize the perimeter of the fluid and grain area. In Fig. 6(a) five of these points are shown at some typical situation. Motion is from the air side towards the fluid side. Technically speaking, the fundamental information that needs to be

stored at each point is the co-ordinates and the accumulated particle mass associated with each respective point. In principle all other quantities may be derived from these, as will be explained in the following.

The accumulated particle mass in a segment of the front is for convenience handled as a volume, the total volume of fluid and particles, which is filled by a dense packing of these particles. Numerically this corresponds to normalizing the particle fraction to one in the dense region within the front. We denote the volume of the point with index i by V_i. Further, we denote the distance between neighboring points, which is easily calculated, by l_{ij}, where i and j are neighbors. The plate separation Δz is fixed and thus the width of the front in a point can be calculated. For point 3 in Fig. 6(a), the front width becomes

$$L_3 = \frac{V_3}{\Delta z(l_{23}/2 + l_{34}/2)}, \tag{14}$$

where the front length associated with the point is the sum of the two half distances to its two neighbors. The resulting front width is illustrated with a vector pointing towards the fluid side in the figure. The orientation of the vectors is always normal to the front. In the case of point 3, one sees how the vector is aligned along the dashed line. This line divides the angle $\angle 234 = 2\beta$ exactly in two equal angles β.

The orientation is only dependent on the point itself and its two nearest neighbors. Also in the case of curvature, we choose to evaluate it locally, only using the nearest neighbors. The curvature κ_c is approximated by, again for point 3,

$$\kappa_{c,3} = \frac{1}{R_{c,3}} = \frac{\pi - 2\beta}{l_{23}/2 + l_{34}/2}. \tag{15}$$

Recall that the curvature, equal to the inverse radius of curvature, is a change in tangential orientation (angle change) per arc length. The approximation consists in using the two straight line segments as a measure of the arc length.

The information calculated so far suffices to evaluate all points in a given configuration and to select the point which yields first. Once selected, the point in question is moved a tiny step inwards, normal to the front. In this study we have chosen this step to be $\Delta s = 3$ μm, which should be compared with the initial spatial resolution of the line: neighbor point distance $l_{\text{init}} = 1.5$ mm. The latter should be small enough to resolve the final structure of the pattern. The displacement step was chosen to be sufficiently small compared with l_{init} in the sense that the measured results did not depend on its value. Some tests were performed to check for this.

The moved point gathers volume (or mass or particles, depending on the perspective) on its way. Although the front is represented as a line, we keep in mind the fact that it is the inner side of the actual front that gathers particles. The increase in volume, again for point 3 in Fig. 6, becomes

$$\Delta V = \frac{\phi_{\text{local}}}{1 - \phi_{\text{local}}} \Delta s \left(\frac{l_{23}}{2} + \frac{l_{34}}{2} \right), \tag{16}$$

where ϕ_{local} is the local volume fraction associated with the position of the point, to be defined below. Note that when point 3 is moved to give the situation in Fig. 6(b), only its own mass is changed. However, the front lengths of points 2, 3, and 4 are changed, from which the front widths L of these points must be recalculated. The same is true for orientation and curvature of these three points.

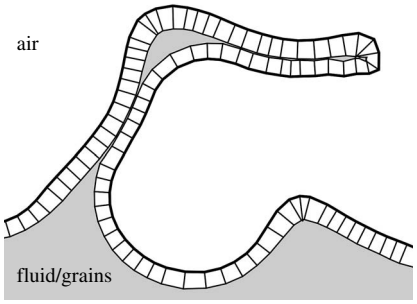

FIG. 7. Snapshot of a section of a simulation. The thicker line towards the air side (white area) is the numerically stored line. A branch of grains is formed when the inside of the front comes in contact with a counterpart segment.

The simulation is implemented with an average spatial volume fraction of mass that represents the filling of grains in the Hele-Shaw cell. Disorder is included by locally allowing the volume fraction of mass to fluctuate around the average value. To estimate the local fraction, the average fraction is multiplied by a number within $I = (1-\epsilon, 1+\epsilon)$. In this study we chose to place a 120×120 virtual lattice of random numbers, which are elements in I, on top of the initial disk. The number of a given point in space is then taken as the linear interpolation between its four nearest lattice points.

In order to maintain a constant spatial resolution, new points are added to the interface as it stretches. Numerically, a limit is set at $1.1 \times l_{\text{init}}$. Whenever two neighbors come further apart a new point is inserted in between, equally distant from each point. Along the line of possible points of equal distance, the one point is chosen which conserves the curvature. Generally, this can be done exactly only for the left neighbor or the right neighbor separately. In the case of differing positions, when calculated for each of the sides independently, a middle position is used.

Volume must be preserved upon insertion of new points. Volume from the two neighbors is transferred to the new point. Imagine a point number 6 being added to the chain in Fig. 6 between points 2 and 3. The volume transfer from points 2 and 3 to 6 then becomes

$$V_6 = -\Delta V_2 - \Delta V_3 = \frac{1}{2}\frac{V_2 l_{23}}{l_{12} + l_{23}} + \frac{1}{2}\frac{V_3 l_{23}}{l_{23} + l_{34}}. \tag{17}$$

Now, the front thickness L, the orientation, and the curvature are calculated anew for points 2, 3, and 6.

The process of moving points and gathering mass continues as long as there are points left that are allowed to move. Points whose extended front of mass comes in mutual contact are immobilized as this represents the formation of a branch of close-packed grains. Figure 7 shows a section of the front during the formation of a branch. The white area is air and the shaded area is fluid and particles. Note how the small pocket of isolated fluid and particles within the particle branch resembles the experimental situation. This area will

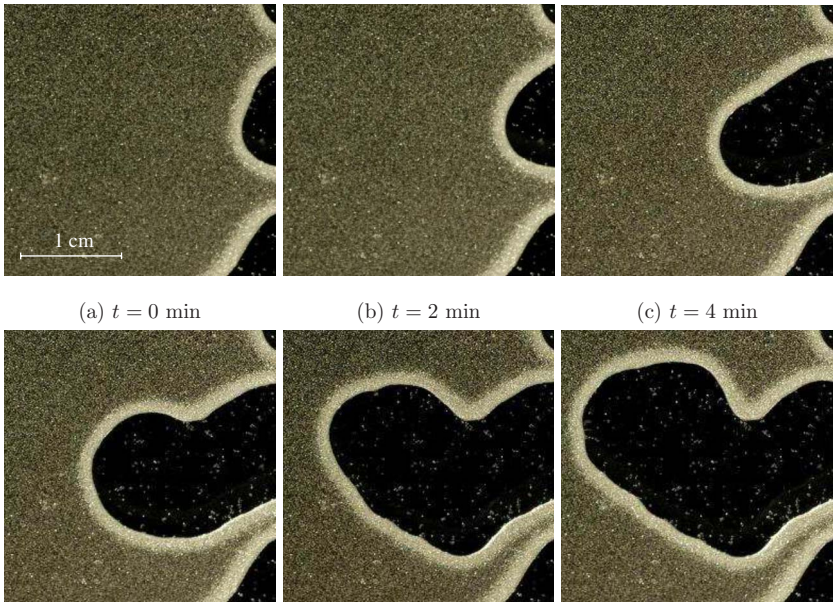

(a) $t = 0$ min (b) $t = 2$ min (c) $t = 4$ min

(d) $t = 6$ min (e) $t = 8$ min (f) $t = 10$ min

FIG. 8. (Color online) Growth of a finger: a 2.7 cm $\times$ 2.7 cm section of the cell is shown for six different times. During these 10 min the active part of the interface, the moving part, was mainly localized within this section.

be drained later when all easier parts are drained, and the pressure difference between fluid and air increases.

IV. THEORETICAL PREDICTION OF THE CHARACTERISTIC LENGTH SCALE

The theoretical prediction for the characteristic width of the fingers will follow from a force balance argument where we assume that the fingers are moving straight and have a tip of circular shape (see Fig. 8). To start we show that the notion of steadily advancing fronts of such circular shape and constant layer width L is consistent with the process of mass accumulation in our system.

A. Mass accumulation along the front and the resulting interface width

Consider the steady state situation illustrated in Fig. 9, where the circular front moves along at velocity u through the medium of solid fraction $\phi \leqslant 1$. The packing fraction ϕ is here defined as 1 for the compact grains in the branches. *A priori*, L should be considered a function of the angle Θ.

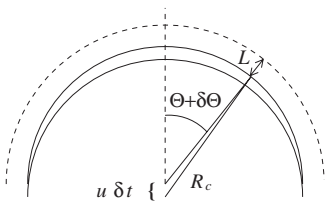

FIG. 9. Model of the fluid-air interface as a circular front behind a close-packed region of width L. The finger defined by this front moves with velocity u. The angle from the center of the circle to a given particle on the interface changes from Θ to $\Theta + \delta\Theta$ during the time δt.

Since the pressure, capillary, and friction forces all act perpendicular to the front, particle displacements will be in the perpendicular direction too, and this will cause distinct particles to move apart. Note that without mass accumulation, area conserving stretching would give $LR[\dot{\Theta}(\Theta+\delta\Theta) - \dot{\Theta}(\Theta)] + \dot{L}R\delta\Theta = 0$. This stretching and the mass accumulation will govern the change of L during a short period of time δt according to the following equation

$$\delta L = \frac{\phi}{1-\phi} u \cos\Theta \delta t - L\frac{\partial\dot{\Theta}}{\partial\Theta}\delta t, \tag{18}$$

where $\dot{\Theta}$ is the time rate of change of the angle to a given particle at the front. The first term describes mass accumulation and the last term describes the effect of stretching. Since δL is a co-moving quantity, i.e., it measures the front width at a position fixed to a particle, we must write

$$\frac{\delta L}{\delta t} = \dot{\Theta}\frac{\partial L}{\partial\Theta} \tag{19}$$

in steady state. Combining this expression with Eq. (18) and grouping terms we get

$$\frac{\partial(\dot{\Theta}L)}{\partial\Theta} = \frac{\phi}{1-\phi} u \cos\Theta, \tag{20}$$

or, by integration

$$\dot{\Theta}L = \frac{\phi}{1-\phi} u \sin\Theta. \tag{21}$$

Working out $\dot{\Theta} = \delta\Theta/\delta t$ is straightforward. From the figure it is seen that $R_c\delta\Theta = u\delta t \sin\Theta$, and therefore $\dot{\Theta} = u\sin\Theta/R_c$, and

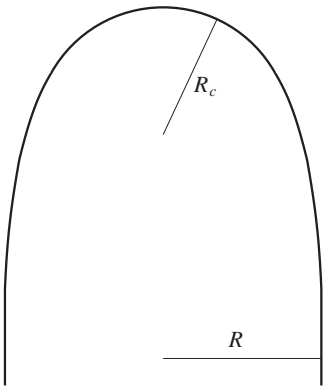

FIG. 10. An advancing fjord is characterized by two lengths, the radius of curvature at the tip R_c and the half width at the straight regions R.

$$L = \frac{\phi}{1-\phi} R_c. \tag{22}$$

This simple result shows that a circular front accumulates mass onto a compacted layer of constant thickness, as long as the front motion is given by forces in the normal direction to the interface. The fact that L takes the above form *after* the front has passed, however, follows directly from mass conservation. The above proof goes to demonstrate that L may in fact be constant along the front.

B. Force balance

Note that a larger ΔP is required to overcome the capillary pressure drop γ/R_c at the tips than along the straighter sides of the fjords. We therefore model the advancing fjord as shown in Fig. 10 which shows a widening of the fjord behind a tip of constant curvature.

Taking $a=1$ and $\tan\theta=1$ here and throughout, we may then write the force balance on the front as

$$\Delta P \leqslant \frac{g\rho\Delta z}{2\kappa}\left[(\kappa\mu+1)\exp\left(\frac{2\mu\kappa L}{\Delta z}\right)-1\right]+\frac{\gamma}{R_c}. \tag{23}$$

At points where the front is moving the "$\leqslant$" sign is replaced by equality. Local conservation of mass again gives

$$L' = \frac{\phi}{1-\phi} R, \tag{24}$$

where L' is the front width along the straight segments. The characteristic wavelength of the maze pattern is then identified as the average fjord plus land width and may be written

$$\Lambda \equiv 2(R+L') = \frac{2}{1-\phi} R. \tag{25}$$

The fact that the fluid pressure drop must be the same across straight and curved segments of the interface allows us to write

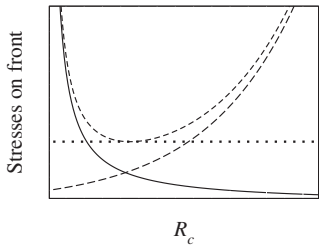

FIG. 11. A sketch of the stresses acting across the front as a function of the radius of curvature R_c at the advancing tip. The solid line shows the surface tension pressure, the long-dashed line shows the frictional stress, and the short-dashed line shows their sum. The dotted line shows the pressure difference ΔP needed to move the front.

$$\Delta P = \frac{g\rho\Delta z}{2\kappa}\left[(\kappa\mu+1)\exp\left(\frac{2\mu\kappa\phi R_c}{\Delta z(1-\phi)}\right)-1\right]+\frac{\gamma}{R_c} \tag{26}$$

for the pressure drop across the finger tips, and for the straight segments

$$\Delta P = \frac{g\rho\Delta z}{2\kappa}\left[(\kappa\mu+1)\exp\left(\frac{2\mu\kappa\phi R}{\Delta z(1-\phi)}\right)-1\right]. \tag{27}$$

The experiment will start by a steady increase in ΔP before the front starts to move. A fjord, or finger, with a small value of R_c will have to overcome a large capillary pressure difference, while a large value of R_c will imply a large value of the front thickness and thus a large friction force. As ΔP is increased from 0, there will initially be no motion. Then a fjord will form with a radius that minimizes the opposing forces, as is illustrated in Fig. 11. This radius will thus minimize $\Delta P(R_c)$ as given by Eq. (26), i.e.,

$$\frac{\partial \Delta P}{\partial R_c} = 0, \tag{28}$$

which may be written

$$R_c = \left(\frac{\gamma(1-\phi)}{g\rho\mu\phi(\kappa\mu+1)}\right)^{1/2}\exp\left(-\frac{\mu\kappa\phi R_c}{\Delta z(1-\phi)}\right). \tag{29}$$

This equation in R_c has the solution

$$R_c = \frac{\Delta z(1-\phi)}{\kappa\mu\phi}\mathrm{W}\left[\left(\frac{\gamma\mu\kappa^2\phi}{g\rho(1-\phi)(\kappa\mu+1)(\Delta z)^2}\right)^{1/2}\right], \tag{30}$$

where W is Lambert's W function, i.e., the inverse function of $y=xe^x$.

By equating the right hand sides of Eqs. (26) and (27) we may solve directly for R in terms of R_c. The result is more instructive, however, if we also use Eq. (28) to simplify it. Equation (28) may also be written as

$$\frac{\gamma}{R_c} = R_c\frac{g\rho(1+\kappa\mu)\mu\phi}{1-\phi}\exp\left(\frac{2\mu\kappa\phi R_c}{\Delta z(1-\phi)}\right). \tag{31}$$

Using this expression to get rid of the γ/R_c term the equality of the right hand sides of Eqs. (26) and (27) takes the form

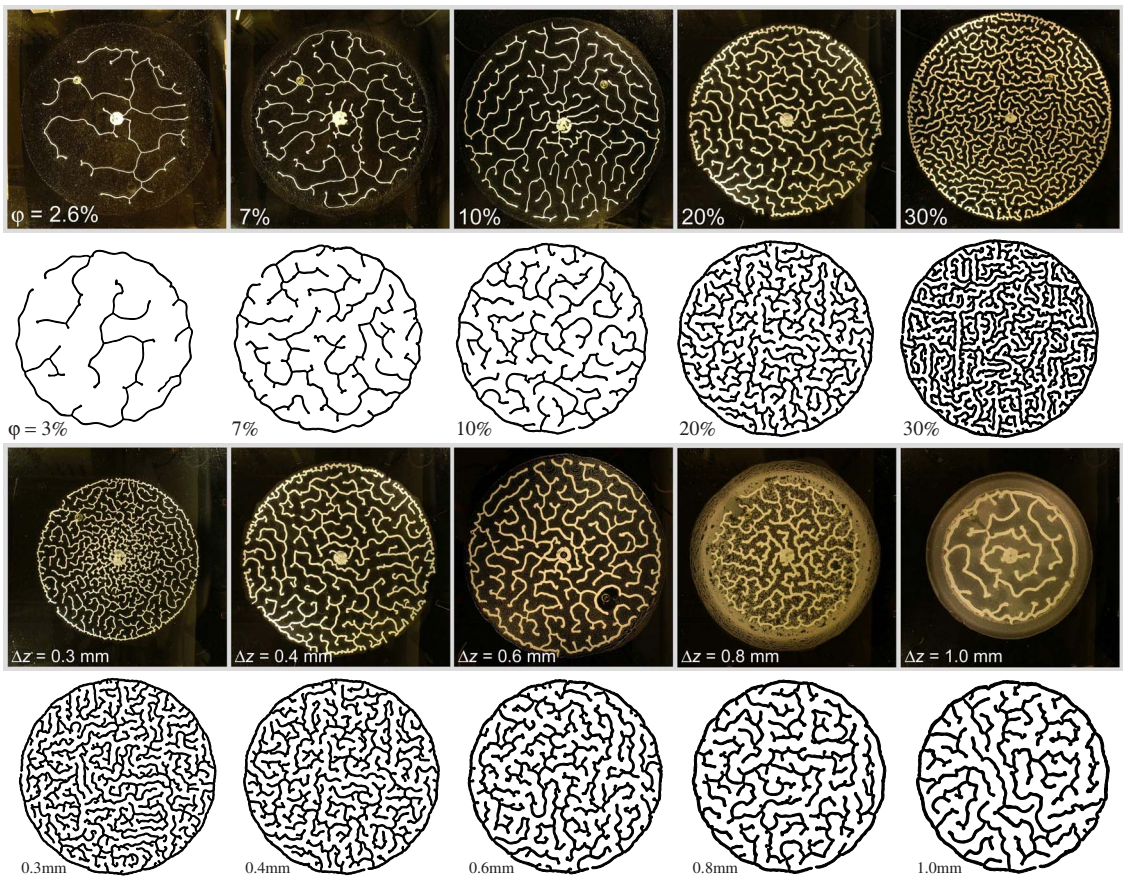

FIG. 12. (Color online) Top two figures: Experimental and simulated structures at different volume fractions and a constant plate separation of 0.4 mm. The volume fraction of grains in the mixture increases from left to right as labeled in the pictures. Bottom two figures: Experimental and simulated structures for different plate separations with ϕ kept constant at 20%. In the experiments, the dimensions of each picture frame are 40×40 cm.

$$\left(1+\frac{2\mu\kappa\phi R_c}{(1-\phi)\Delta z}\right)\exp\left(\frac{2\mu\kappa\phi R_c}{(1-\phi)\Delta z}\right)=\exp\left(\frac{2\mu\kappa\phi R}{(1-\phi)\Delta z}\right) \tag{32}$$

which immediately reduces to

$$R=R_c+\frac{\Delta z(1-\phi)}{2\mu\kappa\phi}\ln\left(1+\frac{2\mu\kappa\phi R_c}{(1-\phi)\Delta z}\right). \tag{33}$$

This result shows that the difference between R and R_c is proportional to Δz. In other words, the displacement between the front of constant curvature and the flat front, as is assumed in the theoretical model and illustrated in Fig. 10, is proportional to the plate separation. This is no big surprise, of course, as the friction force increases exponentially over the characteristic scale of Δz. However, the remaining factors in the Δz term are so large that it cannot be neglected. For instance, for the typical parameter values $\phi=0.2$, $\Delta z=0.4$ mm, $\mu=0.47$, $\kappa=0.8$, $R_c=1$ cm, the above formula gives $R=R_c+9.3\Delta z=(1+0.37)$ cm.

The wavelength Λ now follows directly from Eq. (25) and may be written

$$\Lambda=\frac{2R_c}{1-\phi}+\frac{\Delta z}{\mu\kappa\phi}\ln\left(1+\frac{2\mu\kappa\phi R_c}{(1-\phi)\Delta z}\right). \tag{34}$$

This is the result we will use for the comparison with experiments and simulations.

V. RESULTS AND COMPARISON

As a general observation, the labyrinth patterns are each defined by a single characteristic length scale that is uniform throughout the space filled by the structure. The pattern forming process is a result of local mass transport, and since no pinch-off of the interface occurs during the experiment, the interface remains, topologically, a deformed circle. Consequently, both the fingers and grain cluster are simply connected. The randomness seen in the final pattern arises from the symmetry breaking associated with fingers turning left or right as the patterns are formed. Although disorder is present in the experiment, simulations with no initial disorder (other than the floating point round-off errors intrinsic to the calculations) show that the disorder in the final pattern is a result of chaos, at least in the sense of sensitivity to the initial conditions in the local packing fraction.

Figure 12 shows the structures at different volume fractions and plate separations. The observed decrease in the

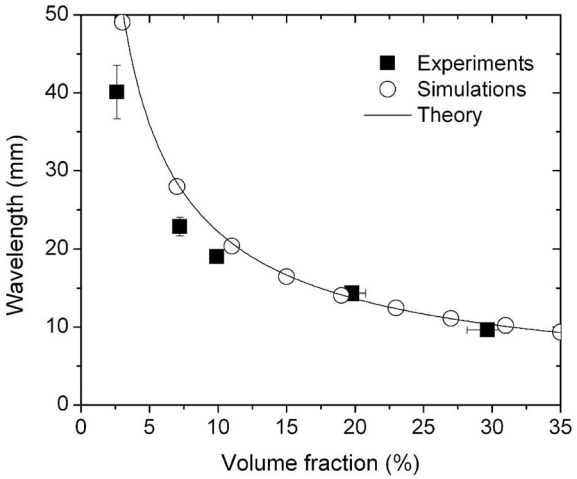

FIG. 13. Wavelength as function of volume fraction.

length scale of the pattern with increased volume fraction is reproduced in the simulations. Using image analysis we isolate the cluster of grains in each picture and measure the characteristic wavelength

$$\Lambda = \frac{2A_{disc}}{S}, \tag{35}$$

where S is the circumference of the cluster of grains and A_{disc} is the area of the initial circular disc of fluid. The measured wavelength for the experiments with lowest and highest volume fraction is 40.1 and 9.6 mm, respectively. The measurements also show a slight thickening of the branches with increasing volume fraction.

In Fig. 13 Λ is shown as a function of mass fraction ϕ, and in Fig. 14 Λ is shown as a function of Δz. The visual resemblance between the experiments and simulations is generally convincing, and a strong indication that the main mechanisms at play are in fact well captured by the model. The most convincing result is that the overall ϕ dependency is very similar for the two cases.

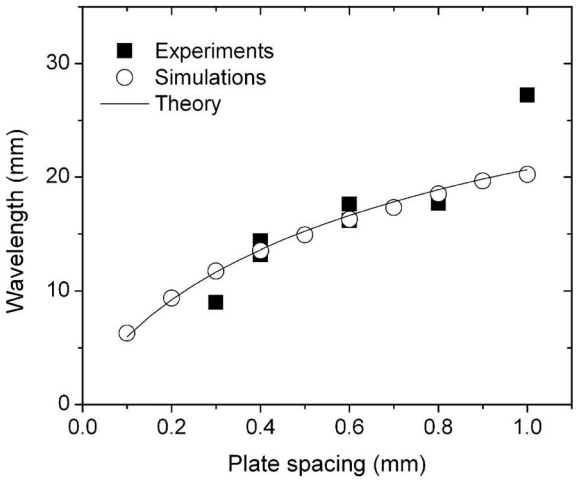

FIG. 14. Wavelength as function of plate separation.

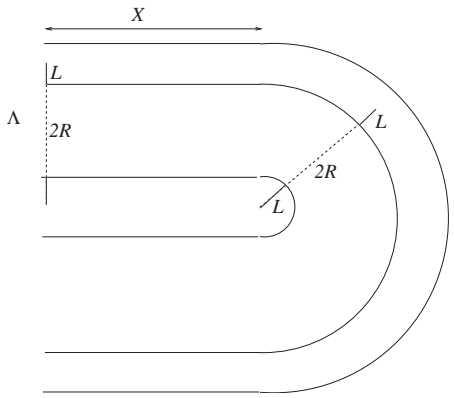

FIG. 15. Sketch of a straight and a curved fjord segment.

However, we note discrepancies between model and experiments at small ϕ and large Δz. The effective friction coefficient in the confined granular system is inherently difficult to estimate accurately, and we have therefore used a value (μ=0.47) that fits the experimental results at high volume fraction. As we have noted above, there is also some uncertainty linked to the value of γ. The effect of impurities in the system is to lower the surface tension, and we have chosen the value γ=0.060 N/m, which is somewhat lower than pure water (0.072 N/m) and pure glycerol (0.064 N/m).

At low ϕ the simulations produce somewhat higher Λ values than in the experiments, possibly due to the friction law providing a less accurate description when the width of the compact layer L becomes comparable to the plate spacing. It is possible that the friction becomes larger for thinner layers (thus giving smaller Λ values) because the internal, rolling degrees of freedom are suppressed. In the simulations the circumference is largely intact, while in the experiment there is more fine scale structure, in particular along the external perimeter. This is most likely caused by a larger noise level in the experimental packing density than in the simulations. The discrepancy at high plate spacing is mainly attributed to an additional effect that becomes noticeable in the experiments as the plate separation approaches the capillary length of the fluid: the meniscus is no longer able to move the granular layer as a whole, and leaves behind a monolayer of beads on the lower plate. This layer is visible in the pictures for Δz=0.8 and 1.0 mm. As a result, the experiments at high plate spacing are less well defined, and a high uncertainty is associated with the measured wavelengths. Apart from this, the quantitative agreement between simulations and experiments is satisfactory throughout.

While the simulations and theory are based on the minimization of the same force function, the theory contains none of the geometric complexity that emerges from the simulation model. Hence the agreement between the two indicates that the length scale is insensitive to the tortuosity of the patterns. This may be understood—at least in part—from the operational definition of Λ, Eq. (35), and the way it measures the same fjord width in curved and straight segments. Figure 15 shows the areas of a straight fjord segment, and a segment that curves an angle of π. The area of the first segment is $A=2X(R+L)$ with a corresponding circumference $S=2X$. For

the curved segment $A=2\pi(R+L)^2$ with a corresponding circumference $S=2\pi(R+L)$. In both cases the definition of Eq. (35) gives $\Lambda=2(R+L)$. This means that the Λ measurements from simulations are suited to reproduce the theoretical prediction, also when they come from curved segments.

VI. CONCLUSION

In conclusion we have explained a pattern forming drying process in terms of only two competing forces, the capillary and friction forces. As such the process appears very simple. Yet, it displays intriguing geometric complexity, characterized by randomness that emerges from the sensitivity to initial conditions in the dynamics of the system. The patterns are mazes, and since the solid phase is simply connected in a topological sense, there is always a way out of the maze.

The structure of the solid phase is compact, i.e., it has a constant average mass density on length scales larger than Λ. However, this does not prevent the structure from being a nontrivial hierarchical branch structure. Work is in progress in our group to study the scaling behavior of this branching structure.

The agreement between the experiments and the simulations is very good apart from some extreme points, i.e., the largest plate separation (Fig. 14) and the smallest volume fraction (Fig. 13). In the latter situation the length L becomes comparable to the plate separation, and we expect our modeling of the granular stress (Fig. 5) to be less accurate. In addition, the hydrostatic effects, which are neglected in the simulations, become increasingly important for large plate separations.

More precisely, the simulations follow the motion of the entire particle front as it deforms, gathers more mass on its way, and stretches, until the whole system is drained. Running series of simulations has allowed us to confirm the theoretical understanding of the problem as well as to span parameter space, identifying and investigating the dependence on central parameters in the problem.

The visual similarity between the present labyrinth patterns and patterns observed in biological systems, such as brain corals, ferrofluids injection processes, and reaction-diffusion systems, raises the intriguing question of a deeper, more general connection.

ACKNOWLEDGMENTS

We thank Dragos-Victor Anghel, Stephane Santucci, Grunde Løvoll, and Joakim Bergli for discussions. We gratefully acknowledge support from the Norwegian Science Foundation under the Petromaks, Nanomat, and SUP grants.

[1] D. Thompson, *On Growth and Form* (Cambridge University Press, Cambridge, England, 1961).
[2] P. Ball, *The Self-MadeTapestry. Pattern Formation in Nature* (Oxford University Press, New York, 1999).
[3] I. Stewart, *What Shape is a Snowflake? Magical Numbers in Nature* (Weidenfeld & Nicolson, London, 2001).
[4] M. C. Cross and P. C. Hohenberg, Rev. Mod. Phys. **65**, 851 (1993).
[5] L. Paterson, Phys. Rev. Lett. **52**, 1621 (1984).
[6] B. Sandnes, H. A. Knudsen, K. J. Måløy, and E. G. Flekkøy, Phys. Rev. Lett. **99**, 038001 (2007).
[7] K. J. Lee, W. D. McCormick, Q. Ouyang, and H. L. Swinney, Science **261**, 192 (1993).
[8] D. M. Petrich and R. E. Goldstein, Phys. Rev. Lett. **72**, 1120 (1994).
[9] R. E. Rosensweig, M. Zahn, and R. Shumovich, J. Magn. Magn. Mater. **39**, 127 (1983).
[10] Y. Yamazaki and T. Mizuguchi, J. Phys. Soc. Jpn. **69**, 2387 (2000).
[11] H. Nakanishi, R. Yamamoto, Y. Hayase, and N. Mitarai, J. Phys. Soc. Jpn. **76**, 024003 (2007).
[12] Y. Yamazaki, S. Komura, and K. Suganuma, J. Phys. Soc. Jpn. **75**, 043001 (2006).
[13] S. Komura and Y. Yamazaki, J. Phys. Soc. Jpn. **76**, 083801 (2007).
[14] H. S. Hele-Shaw, Nature (London) **58**, 34 (1898).
[15] H. A. Janssen, Z. Vereins Dtsch. Ing. **39**, 1045 (1895).